Ultrasonic Spectrum Analysis for Tissue Assays and Therapy Evaluation

Frederic L. Lizzi,[1] Michael Astor,[1] Tian Liu,[1] Cheri Deng,[1] D. Jackson Coleman,[2] Ronald H. Silverman[2]

[1]Riverside Research Institute, 330 West 42nd Street, New York, NY 10036

[2]Cornell University Medical College, 1300 York Avenue, New York, NY 10021

ABSTRACT: Ultrasonic spectrum analysis procedures have been developed to measure tissue morphologic features that are not well depicted with conventional ultrasonography. This article reviews some of the applications of spectral techniques and provides an expanded theoretical framework showing how measured spectral features are related to the spatial autocorrelation function descriptive of tissue microstructure. Explicit relationships are obtained that describe how linear-regression spectral parameters are related to the effective mean sizes, concentrations, and relative mechanical properties of scattering centers in tissue. *In vitro, in vivo,* and clinical results are presented illustrating how these techniques can be used to evaluate tissue alterations induced by ultrasonic hyperthermia and ablative treatments of tumors. These results show that ultrasonic spectrum analysis can provide quantitative information regarding changes in microstructure attributes. Spectral parameter images in two and three dimensions demonstrate how such procedures can map the spatial extent and severity of these changes, thereby providing a quantitative basis for assessing the results of tumor therapy. © 1997 John Wiley & Sons, Inc. Int J Imaging Syst Technol, **8,** 3–10, 1997

I. INTRODUCTION AND BACKGROUND

Pulsed-echo ultrasonic imaging has become a standard procedure in medical practice, and advances continue to be made in producing highly detailed images of tissue structures. It has long been realized that despite the clinical utility of ultrasonic B-mode images, conventional systems do not extract all of the information about tissue microstructure that is contained in received echo signals. These systems have been designed to provide high-quality images based on video signals, which are estimates of the envelopes of the coherent radio-frequency (rf) echo signals returned from the body. As described below, theoretical and clinical studies have shown that alternative spectral processing of rf echo signals can provide complementary information about fine-scale tissue features, which are not well characterized by conventional imaging.

Ultrasound energy interacts with soft tissues in a diversity of ways, and ultrasonic imaging is affected by phenomena not encountered to a significant degree with other medical imaging modalities such as X radiation and magnetic resonance. Ultrasonic imaging is more closely related to sonar, radar, and laser imaging technologies. Ultrasonic systems [1] employ short pressure pulses, typically comprising two cycles of alternating compression and rarefaction with respect to ambient pressure; these bipolar pulses are launched by focused transducers (or transducer arrays) usually operated at center frequencies near 5 MHz (0.3-mm wavelength). The pulses propagate relatively slowly (1.5 mm/μs) through soft tissues, where they are affected by diffraction, acoustic attenuation, and refraction. Scattering occurs when a pulse encounters changes in the mechanical properties (density and compressibility) of tissue constituents. Backscattered echo pulses are sensed in a coherent fashion by the transducer, which generates an output rf voltage signal proportional to the instantaneous ultrasonic pressure averaged over its receiving aperture.

Simple tissue interfaces, such as organ boundaries, produce well-defined rf echo signals whose video envelopes are clearly imaged in B-mode displays. However, most structures of interest (e.g., organ parenchyma, tumors, hemorrhages) contain a complex spatial distribution of mechanical properties due to their complex internal microstructure. Echo signals from these structures exhibit complicated interference patterns arising from closely spaced scattering centers, which are not resolved because their constituent echoes overlap in time. B-mode images reflect this underlying complexity, exhibiting an average gray-scale level (indicative of average scattering strength) with a superimposed speckle pattern. [2] Speckle patterns consist of randomly positioned bright and dark spots resulting from the coherent interference among echo constituents. Clinicians interpret such images on the basis of boundary geometry, internal brightness (''echogenicity'') and ''spatial texture,'' and shadowing or antishadowing of posterior regions (due to elevated or lowered attenuation coefficients in different types of tumors).

A number of investigators have examined techniques to im-

prove upon these conventional imaging procedures and thereby provide a more objective basis for tissue assays [3]. Frequently, these investigations have employed frequency-domain approaches which facilitate the description of tissue-ultrasound interactions and also simplify compensation for extraneous system artifacts. In addition, many of these alternative examination techniques incorporate statistical methods to describe complex tissue microstructures.

Frequency-domain implementations usually employ spectrum analysis of coherent rf signals from temporally gated tissue segments, and they derive average spectra that describe the mean properties of tissues lying within well-defined spatial regions; spectral-parameter imaging has also been employed using sliding analysis gates to generate cross-sectional images of frequency-domain features. Relevant fundamental studies have been conducted in the laboratories of Reid [4], Shung [5], Waag [6], and Ophir [7]. Miller and coworkers [8,9] reported extensively on integrated backscatter, a parameter that measures the area under the calibrated rf spectra (in decibels). They showed how this parameter is related to tissue features, and how it can be applied to quantitative assays of cardiac ischemia. Zagzebski and coworkers [10] applied spectral processing to characterize liver structures, and Insana and co-workers [11] used spectral processing to quantify microstructure in the kidney.

Our investigations have been aimed at developing ultrasonic spectral methods to improve diagnosis, treatment planning, and treatment monitoring. Our methods have been applied to clinical assays of the prostate, liver, blood vessels, and the breast [12–15]. This report treats our results in ophthalmology, where noninvasive procedures are critical because biopsies are usually precluded. Studies in the eye pose demanding problems because of the small sizes (e.g., 5 mm) of ocular tumors. However, the eye is a model organ for ultrasonic studies since it permits high-frequency, broad-bandwidth examinations with little intervening attenuation, which would otherwise alter spectral features.

Over the years our ophthalmic studies have addressed a variety of interrelated topics which have provided useful information for studies of other organs. First, we developed a theoretical scattering model that relates spectral features to the effective physical attributes of complex tissue microstructures [16,17]. While these attributes are rigorously described in statistical terms (e.g., autocorrelation functions), we have found it useful to discuss them in terms of effective scatterer size and acoustic concentration. Acoustic concentration is defined as CQ^2, where C is the effective concentration of scatterers and Q is their relative acoustic impedance (product of density and speed of acoustic propagation) with respect to that of the surround. Second, we developed clinical databases showing how spectral parameters can identify different types of ocular tumors and subclassify them in groupings associated with lethality potential [18,19]. We also used clinical follow-ups of over 10 years to show how these parameters could be used with ancillary information (e.g., tumor size) to predict survival times following alternative therapies [20]. Third, we showed how spectral parameters can sense subtle microstructural alterations induced by radiotherapy and ultrasonically induced hyperthermia [21]. To expedite the interpretation of clinical results, we developed quantitative imaging procedures [18,22] that depict spectral parameters and scatterer sizes and acoustic concentration in two-dimensional and three-dimensional (3D) formats. We have recently undertaken a program to extend our spectral and imaging methodologies to very high center frequencies (e.g., 50 MHz)

with commensurately large bandwidths [23] to study diseases such as glaucoma, which affect tissue structures with total dimensions under 1 or 2 mm.

As discussed in this report, we are currently expanding our studies of spectrum analysis procedures for therapy monitoring to guide the use of new therapeutic procedures. As an example, noninvasive means are required to delineate the size, geometry, and severity of localized therapeutic lesions induced in tumors by focused ultrasound [24]. Similar needs exist for evaluating ultrasonic hyperthermia which is employed to treat larger tissue volumes [25]. Ultrasonic spectral procedures that can sense microstructural features promise to meet these needs; such applications may in fact be more tractable than differential diagnosis because changes in spectral parameters, rather than their absolute values, are of interest in treatment monitoring. Thus, ancillary problems associated with, e.g., intervening attenuation, are less important in evaluating tissue responses to treatment.

This report reviews the basic formulation of our theoretical scattering model and derives results for stochastic scatterers without previous simplifying assumptions regarding the beam width and gate length. The report also derives expressions that explicitly relate summary spectral features to effective scatterer properties. Finally, it presents illustrative results that demonstrate how these techniques can be applied to monitoring the effects of hyperthermia and ablation.

II. SPECTRUM-ANALYSIS MEASUREMENT PROCEDURES

Our spectrum analysis procedures are applied to digital samples of rf echoes acquired during conventional ultrasonic scanning [16,23]. Along each scan line, rf signals are sampled at a rate exceeding the Nyquist requirement at the highest frequency component of interest. In ocular examinations with a 10-MHz focused transducer (10-mm aperture diameter, 35-mm focal length), rf data are sampled at 50 MHz, and 2 kBytes of data are acquired along each of 128 scan lines. (Technical descriptions of acquisition hardware and software are presented in [23], which also describes higher-frequency data acquisition.) Acquired data are digitally processed using a variety of programs written in C and executed on personal-computer platforms.

The processing sequence begins with the generation of a B-mode cross-sectional image derived from the acquired rf signals. As shown in Figure 1, a region of interest (ROI) is then used to demarcate the tissue segment to be analyzed. Along each scan line segment in the ROI, rf signals are multiplied by a Hamming function and a fast Fourier transform (FFT) algorithm is applied to compute spectra as a function of time or, equivalently, distance. The magnitudes of resultant spectra from each scan line are then squared and averaged to compute an average power spectrum. This spectrum is then divided by a calibration spectrum to remove extraneous system and transducer transfer functions including the spectrum of the launched pulse. The calibration spectrum is obtained from a planar target examined in the transducer's focal plane [16]. The calibrated spectrum $S(f)$ is converted to decibels for display and for determination of summary spectral parameters, which are derived with linear regression procedures.

Calibrated power spectra expressed in decibels are denoted as $S'(f)$ and are analyzed with linear regression techniques over the frequency band determined to afford adequate signal-to-noise ratios (SNR). Typically, this band corresponds to the −15-dB points of the calibration spectrum, and it is numerically equal to
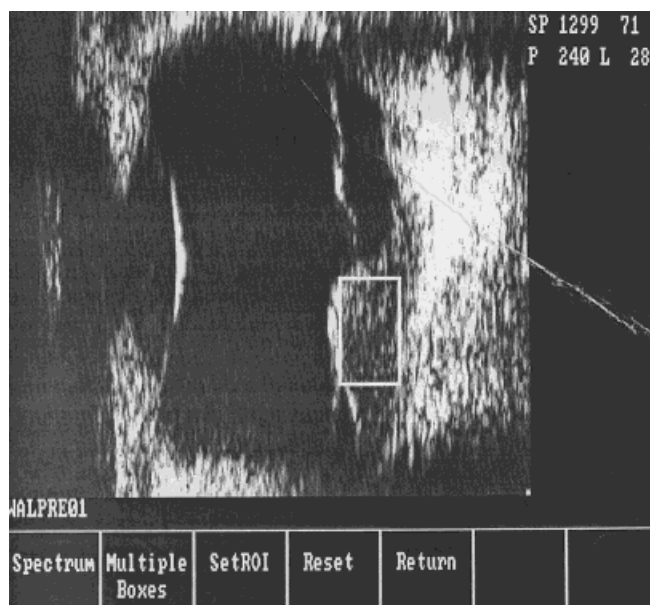
Figure 1. Computer-generated B-mode display of eye showing ROI positioned within a posterior malignant melanoma with adjacent retinal detachment.

Figure 3. Midband-fit image of melanoma within ROI; gray-scale encoding for midband fit (in decibels) shown at right.

the center frequency; in typical ocular examinations, this band extends from 5 to 15 MHz, as shown in Figure 2. Linear regression analysis is employed to compute three summary spectral parameters: spectral slope m (dB/MHz); spectral intercept I (dB, extrapolation to 0 MHz); and midband fit M (dB, value of the
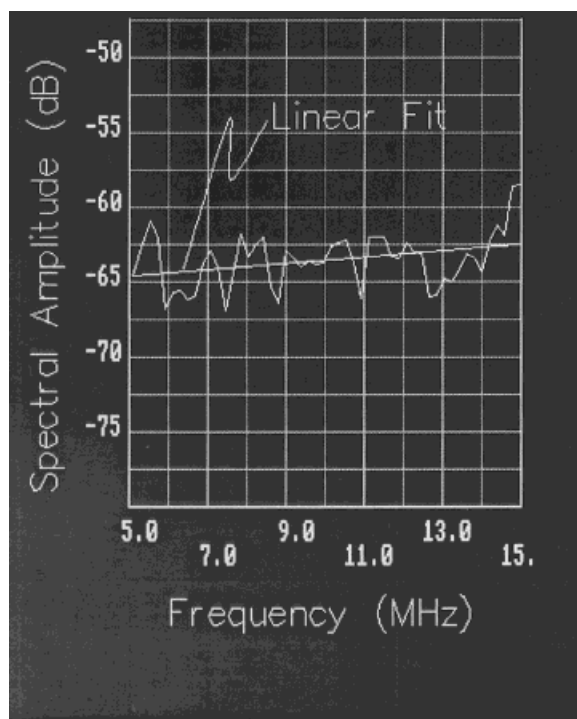

Figure 2. Calibrated power spectrum obtained from rf signals in the ROI shown in Figure 1.
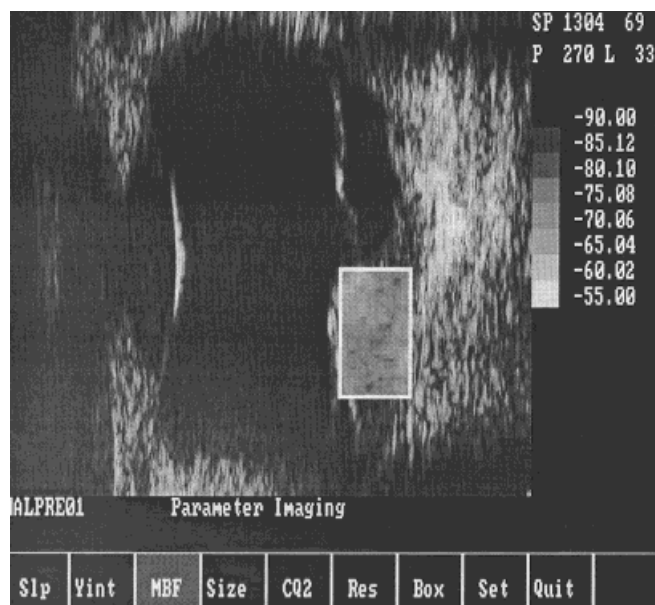
linear fit at the center frequency). Although only two of these parameters are independent, we find it useful to consider all three.

As an alternative to ROI analysis, cross-sectional parameter images [18,22] of the above spectral parameters are generated using a sliding Hamming window to analyze all rf data along each scan line. For 10-MHz ophthalmic examinations, the window length is typically set to 1 mm. Each of the procedures described above is applied to single (i.e., unaveraged) power spectra at each window site. Local values of m, I, and M are computed and displayed as functions of position. As an example, Figure 3 shows a gray-scale image of M within an ROI encompassing the same ocular tumor as shown in Figure 1. Derived estimates of scatterer properties can be imaged in the same manner [18].

Each spectral parameter is related to physical scatterer properties as derived in the next section. Attenuation in intervening tissues can also affect these parameters. To address this topic, we assume that average pressure attenuation coefficient α' (nepers/MHz-cm) is linearly proportional to frequency f (MHz), and we denote the length of traversed intervening tissues by X (cm). Then, the measured calibrated power spectrum is equal to $\exp(-4\alpha'fX)S(f)$ and the measured spectrum in decibels is equal to $S'(f) - 2\alpha fX$, where α is α' expressed in dB/MHz-cm. (The factor of 2 accounts for two-way travel of the pulse through the tissue segment.) The measured spectral parameters (denoted by subscript 1) are related to the ideal values, measured in the absence of attenuation, by the following simple relations where the center frequency is f_c:

$$m_1 = m - 2\alpha X; \quad M_1 = M - 2\alpha f_c X$$

$$I_1 = M_1 - m_1 f_c = M - m f_c = I. \tag{1}$$

Equation (1) shows that the intercept value is not affected by intervening attenuation with a typical, nearly linear dependence on frequency. The next section relates m, I, and M to scatterer

properties, and assumes that αX is negligible. This assumption is reasonable in most ophthalmic examinations, in which transmission occurs through thin ocular walls (small X) and ocular humors (low α); transmission through thick segments of the absorptive lens is avoided for spectral studies. In tissues where this assumption is not applicable, results derived in the next section are still valid, but corrections must be applied to clinical data using Equation (1) and estimates or measurements of αX. Reference [26] describes how Equation (1) can be used to estimate α in extended statistically homogeneous tissues, i.e., tissues which exhibit a range-independent mean value of M; in this case, α can be determined by measuring the linear rate of decrease of M_1 with increasing range X. (This reference also briefly discusses the effects of α with nonlinear frequency dependencies.)

III. THEORETICAL FORMULATION

Our theoretical framework [16,17] for spectrum analysis relates computed power spectra to properties of the examined tissue, measurement system, and analysis parameters. The formulation treats weak scattering (Born approximation) from statistically homogeneous tissue segments located in the focal volumes of moderately focused transducers, which are typically employed in diagnostic ultrasound. Under these conditions, tissue scattering is shown to arise from the spatial gradient of acoustic impedance [16].

Our analysis characterizes tissue structures in terms of a stochastic spatial distribution of acoustic impedance Z, which exhibits small fluctuations about its mean value Z_0. This spatial distribution is assumed to be statistically stationary (wide-sense) so that $(Z - Z_0)/Z_0$ can be described in terms of the spatial autocorrelation function (ACF) $R_\zeta(\underline{\Delta x})$ where the vector $\underline{\Delta x}$ denotes lagged spatial coordinates Δx, Δy, Δz in the x, y, and z directions, respectively. Beam propagation occurs in the x direction.

We have found it useful to assume that the tissue ACF comprises an isotropic Gaussian function [17]

$$R_\zeta(\underline{\Delta x}) = R_\zeta(0)e^{-(1.17(|\Delta x|/\rho)2)} \quad (2a)$$

$$R_\zeta(0) = \tfrac{4}{3}\pi\rho^3 CQ^2 \quad (2b)$$

where ρ defines the ''effective scatterer size'' (radius) as determined by the correlation dimensions of $(Z - Z_0)/Z_0$.

The analysis includes two other ACFs to describe beam and gate functions, respectively. $R_D(\Delta x, \Delta y)$ describes the cross-range ACF of the beam's two-way directivity function, $F^2(y, z)$. For a transducer aperture of radius a and a range R near the focal plane, the following relations [16] apply, where $J_1(\ )$ is a Bessel function of the first kind and first order and where $q = a/R$:

$R_D(\Delta y, \Delta z)$

$$= \left(\frac{k^2a^2}{4\pi R^2}\right)^2 \int_{-\infty}^{\infty}\int_{-\infty}^{\infty} F^2(y, z)F^2(y + \Delta y, z + \Delta z)\,dydz \quad (3a)$$

$$F(y, z) = 2J_1(kqr)/(kqr) \quad (3b)$$

$$r = (y^2 + z^2)^{1/2}; \quad \Delta r = (\Delta y^2 + \Delta z^2)^{1/2} \quad (3c)$$
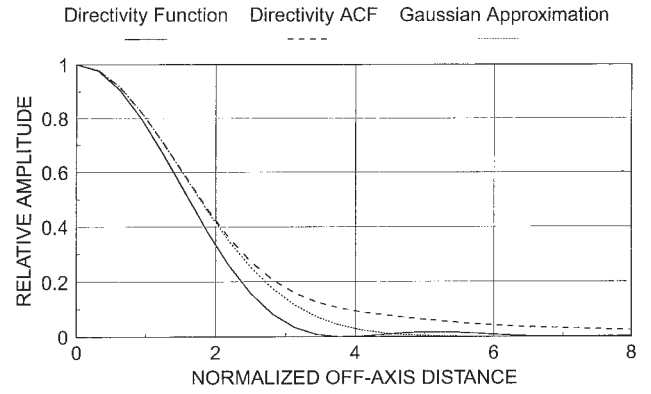
$$R_D(0) = 0.361(k^2q^2/4\pi). \quad (3d)$$

Directivity Function   Directivity ACF   Gaussian Approximation

Figure 4. Plots of beam-directivity function, directivity-function ACF, and Gaussian ACF approximation versus normalized off-axis distance. Plots are normalized to their axial values and plotted as a function of kqr (for directivity function) and $kq\Delta r$ (for ACFs).

The range gating function $g(x)$ is characterized by an ACF, $R_G(\Delta x)$

$$R_G(\Delta x) = \int_{-\infty}^{\infty} g(x)g(x + \Delta x)\,dx. \quad (4)$$

In the current case, $g(x)$ is a Hamming function whose spatial length L is set by the time duration T of the gate; i.e., $L = cT/2$, where c is the average speed of acoustic propagation in the examined tissues. For this function, $R_G(0) = 0.4L$ [17].

Our previous formulation included two simplifying conditions [16,17]. First, the gate-function length was assumed to be extremely long compared to ρ, so that $R_G(\Delta x)$ could be approximated as $R_G(0)$. Second, the beamwidth was assumed to greatly exceed the lateral dimensions (correlation width) of scattering elements; this assumption permitted $R_D(\Delta r)$ to be approximated as $R_D(0)$. This report does not initially make these assumptions, and treats a more general expression for S, the power spectrum for the ensemble of scatterers characterized by R_ζ:

$$S(k) = \left[4k^2 \int_{-\infty}^{\infty} R_\zeta(\underline{\Delta x})R_D(\Delta y, \Delta z)e^{j2k\Delta x}\,d\underline{\Delta x}\right]*$$

$$\times \int_{-\infty}^{\infty} R_G(\Delta x)e^{j2k\Delta x}\,d\Delta x \quad (5)$$

where j represents $\sqrt{-1}$, and the wavenumber k is equal to $2\pi f/c$. The bracketed term in Equation (5) involves tissue and beam ACFs; this term is convolved with the Fourier transform of the gating function's ACF. This frequency-domain convolution (denoted by *) results from the fact that in the time domain, the gating function multiplies the analyzed rf echo signals.

We now treat the bracketed term in Equation (5), which is denoted as $S_0(k)$; this integral involves R_D, the directivity-function ACF. Figure 4 shows a plot of $R_D(\Delta r)/R_D(0)$ evaluated as a function of $kq\Delta R$. As seen in the figure, $R_D(\Delta r)$ can be closely approximated as a Gaussian function:

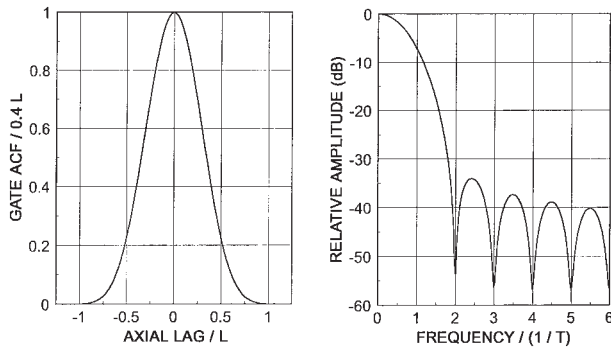$$R_D(\Delta r) \approx R_D(0)e^{-0.22k^2q^2\Delta r^2}. \quad (6)$$

Figure 5. Normalized ACF (left) and power spectrum (right) of Hamming gating function.

This approximation agrees with the actual value of R_D to within 1% of $R_D(0)$ for scatterer diameters as large as the -6-dB beamwidth, which occurs at $kqr = 2.19$; for the current application, this corresponds to a scatterer diameter of 0.8 mm, which is significantly larger than the scatterer sizes of interest, as seen in the following section.

Using the approximation of Equation (6) together with Equations (2) and (5), the power spectrum can be evaluated:

$$S(k) = 4k^2 \left(\frac{\rho}{1.17}\right)^3 \pi^{3/2} \frac{R_\zeta(0)R_D(0)e^{-(k\rho/1.17)^2}}{[1 + 0.16(kq\rho)^2]} * S_G(k) \qquad (7)$$

where $S_G(k)$ is the Fourier transform of the gating function ACF, as indicated in Equation (5).

Using Equation (4), the function $S_G(k)$ can be determined from the ACF of a Hamming function, which is explicitly stated in [17]. Figure 5 plots this ACF and its Fourier transform $S_G(f)$ as a function of normalized temporal frequency. The -3-dB bandwidth B of S_G is found to be approximately equal to $1.13/T$, which corresponds to $1/L$ (where L is specified in millimeters and B in megahertz). In previous treatments, we assumed that L was much larger than the correlation dimensions of the tissue ACF; thus, the bandwidth of $S_G(f)$ was assumed to be small enough that $S_G(f)$ could be approximated as $R_G(0)\delta(f)$, where $R_G(0)$ is evaluated as $0.4L$ and δ denotes a delta function.

We will first apply this assumption regarding R_G to examine the spectra of Equation (7) for long gate durations. Then, we will explicitly address the effects of shorter gate lengths. For long gate lengths, Equation (7) can be rewritten in the temporal frequency domain using Equations 2(b) and 3(d):

$$S(f) = 185Lq^2\rho^6 CQ^2 f^4 \frac{e^{-(3.487f\rho)^2}}{[1 + 2.66(qf\rho)^2]}. \qquad (8)$$

Figure 6 shows plots of this result for typical ocular scatterers with diameters ranging from 20 to 100 μm. For small scatterers (e.g., 20 μm), the exponential term and the denominator of Equation (8) are near unity, so that Rayleigh spectra proportional to f^4 and ρ^6 are observed. As the effective scatterer size increases, the spectra become less positively sloped; for scatterers larger than 80 μm, they can become negatively sloped, i.e., low frequencies are scattered more strongly than higher frequencies.

The effects of convolving these results with $S_G(f)$ will be examined for the Rayleigh scattering case, specifically for a 3-
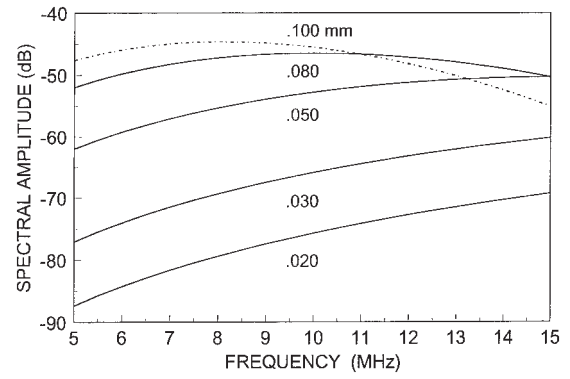

Figure 6. Calibrated power spectra for indicated effective scatterer diameters for typical ocular examination parameters. $CQ^2 = 1$ mm^{-3}.

μm scatterer diameter. This situation presents a rapid change of spectral amplitude with frequency, and it therefore places stringent demands on preserving spectral shape for further analysis. We also include the effects of white electronic noise whose power spectral density is N; the noise is assumed to be uncorrelated with tissue spectra, so that the measured power spectrum is equal to $[S_0(f) + N]*S_G(f)$.

Figure 7 shows results for $S(f)$ for a small value of L (0.3 mm) and for an SNR of 20 dB (SNR is defined here as the ratio of the average value of $S_0(f)$ to N over the typical 5–15-MHz bandwidth). This figure shows that values of L near 0.3 mm artifactually increase the value of spectral components by as much as 3 dB; the largest increases occur at the lowest frequencies because the convolution intermixes large high-frequency spectral components and noise components with the relatively small low-frequency spectral components. Larger values of L produce smaller artifacts, which are still largest at low frequencies. Figure 8 shows the maximum differences between S and S_0 as a function of L for various SNR levels. For typical SNR levels (near 30 dB), values of L that are 0.75 mm or greater produce maximum differences that are smaller than 0.5 dB and do not significantly affect spectral slope, intercept, or midband fit values described in the next paragraph.

For situations where convolution artifacts are not significant, Equation (8) can be evaluated to relate calibrated spectra $S(f)$ to the scatterer parameters ρ and CQ^2. The spectral parameters m,
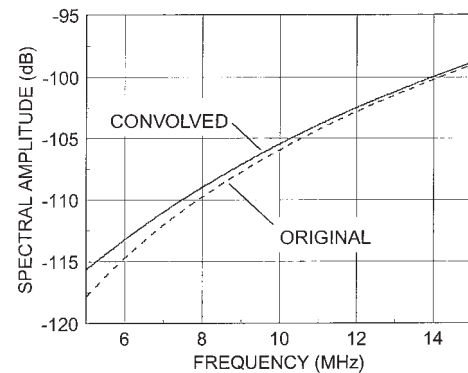

Figure 7. Calibrated power spectra before and after convolution with gate power spectrum. SNR = 20 dB; L = 0.3 mm; effective scatterer diameter = 3 μm.
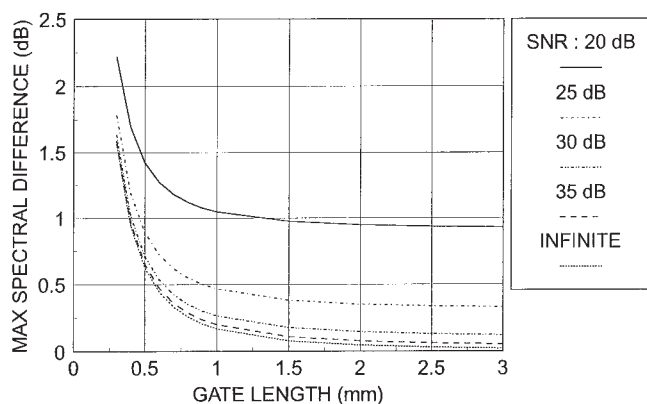
Figure 8. Maximum power spectral difference introduced by convolution with Hamming-gate power spectrum over 5–15-MHz band for indicated SNR levels. Infinite SNR indicates absence of noise.

M, and I can be determined by computing $S(f)$ in decibels for various values of ρ (as in Fig. 6) and then applying linear regression to each spectrum to compute slope, midband fit, and intercept, respectively. This procedure yields the results plotted in Figure 9 for $CQ^2 = 1$ mm^{-3} and the ophthalmic system parameters of the preceding section; L is set to 1 mm. The plots show that all three spectral parameters are affected by scatterer size; M and I are also affected by CQ^2. Quadratic regression analyses of the plots in Figure 9 show that the following approximate relations apply where d denotes the effective scatterer diameter (2ρ) in millimeters and f_c is expressed in megahertz:
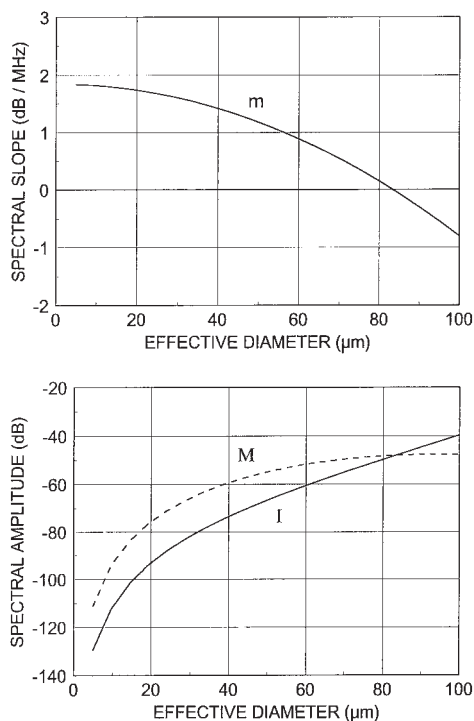

Figure 9. Relationships between effective scatterer diameters and (a) spectral slope m and (b) intercept I and midband fit M, for typical ocular examination parameters and $CQ^2 = 1$ mm^{-3}.

Table I. Pre- and post-treatment values of spectral parameters and derived scatterer properties for ultrasonically induced hyperthermia.

Parameter	Pretreatment	Post-treatment	Change
Slope (dB/MHz)	0.261	−0.147	−0.408
Intercept (dB)	−66.8	−55.3	11.5
Diameter (μm)	77	87	10
CQ^2 (dB re 1 mm^{-3})	−16.04	−8.87	7.17

$$m = 1.85 - 265\,d^2$$
$$I = 58.3 + 114\log(d) + 14.3[\log(d)]^2 + \log CQ^2$$
$$M = I + mf_c. \tag{9}$$

The approximation for m is within 0.1 dB/MHz of the actual slope value, and the approximations for I and M are within about 1.5 dB of actual values.

IV. THERAPY MONITORING RESULTS

This section presents illustrative results showing how spectrum analysis techniques can be employed to assay therapeutic changes produced in tissue structures. We have now applied these techniques to monitor acute and chronic effects of ultrasonically induced hyperthermia and focal ablation of ocular tumors. Hyperthermia uses broad ultrasonic beams to insonify large tumor segments and raise their temperature above 45°C for sustained periods of time [21]. In this case, spectral techniques are used to survey large tissue segments to evaluate changes in mean properties and the spatial uniformity of tissue alterations. Ablation, better termed focal thermal necrosis, employs focused beams to produce rapid changes within small, well-defined tissue volumes; in this case, spectral assays are used to delineate altered regions and to compare spectra in lesioned volumes with surrounding tissue regions.

We have previously reported hyperthermia-induced changes in experiments using nude athymic mice with subcutaneous human tumor explants (in the thigh) [21]. When these tumors grew to the size of human ocular melanomas (5–8-mm thicknesses), they were insonified with the defocused region of a 4.6-MHz beam (1–2 W/cm^2) for 30 min to achieve a 49°C core temperature. The tumors were scanned with our ocular diagnostic system before and immediately after therapy. Table I shows the mean pre- and post-exposure values of spectral slope and intercept for a group of six tumors. The hyperthermia exposure caused spectral slope to decrease by 0.408 dB/MHz and elevated intercept values by more than 10 dB; both changes were significant at the 0.003 level.

We have now employed results from the preceding section to evaluate the corresponding changes in effective scatterer size and acoustic concentration produced by hyperthermia. The spectral slope values indicate [from Eq. (9)] that the mean effective scatterer diameter was increased by 10 μm, from a pretreatment value of 77 μm to a post-treatment value of 87 μm. These diameters and the measured intercept values, used with Equation (9), show that the treatment increased CQ^2 by 7 dB. Based on post-exposure histology, we currently hypothesize that these changes in scatterer properties are associated with the production of interstitial fluid-filled spaces in the tumor. CQ^2 values are increased because of the production of new scattering surfaces (increase in C) and
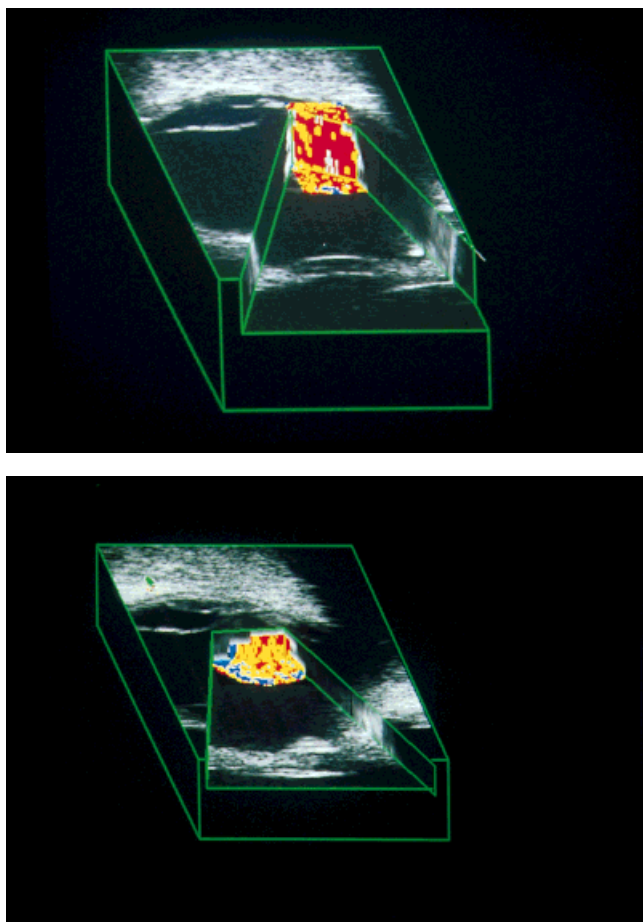
Figure 10. Three-dimensional renderings of ocular melanoma with color-coded spectral intercept values: (a) pretreatment result; (b) post-treatment result. "Slices" are simulated through cornea, lens and tumor. Retinal detachment and posterior orbital fat are displayed in uncut regions.

possibly because Q is elevated at interfaces between interstitial fluid and solid tissue constituents.

Figure 10 shows clinical results for a choroidal malignant melanoma treated with ultrasonic hyperthermia. To obtain three-dimensional (3D) information, this tumor was scanned in a set of 30 parallel planes (separated by 0.5 mm) before and immediately following treatment; rf data were acquired in the usual manner in each plane [22]. Spectral parameter images were then generated in the tumor regions of each scan, and the results were displayed using an interactive "block" format constructed by digitally stacking the images. The figures show spectral intercept level with the following color code: red, -80 to -70 dB; yellow, -70 to -60 dB; blue, ≥ 60 dB. The effects of treatment were assessed by rotating and slicing the pre- and post-treatment images as indicated in Figure 10. Treatment effects were similar to those found in the nude mice experiments. The shift of color from red (pretreatment) to yellow (post-treatment) through most of the tumor volume indicates that therapy has elevated intercept values by about 10 dB, similar to the results in nude mice. (Blue regions in anterior tumor segments correspond to the echogenic overlying retina.)

We have recently applied spectrum analysis to study short-term thermal necrosis produced in *in vitro* liver specimens with a focused therapy transducer. In this case, pre- and postexposure rf data were acquired with the same real-time 10-MHz transducer that was used to position the therapy beam's focal point within the tissue specimen. Figure 11 shows a midband-fit image over an entire sector-scan immediately following a 5-s exposure at a focal point intensity of 700 W/cm^2 (4.1 MHz). The image was compensated for an attenuation coefficient of 0.5 dB/MHz-cm using relationships described in Equation (1). The lesion is characterized by midband-fit levels that are at least 6 dB greater than surrounding levels. Midband fit is also seen to be high in other isolated tissue segments, which may have been the site of small air bubbles, and at the highly echoic interface between the liver specimen and the coupling fluid. We are currently expanding these studies using our *in vivo* tumor model to correlate such spectral changes with lesion severity in ocular tumors.

V. SUMMARY AND CONCLUSION

Calibrated spectrum analysis procedures show the potential of providing key tissue descriptors that can complement high-quality B-mode images. These procedures remove measurement system artifacts and provide objective quantitative parameters descriptive of tissue microstructure. The analysis described in this report provides a theoretical basis for interpreting spectral parameters in terms of physical attributes of tissue morphology. These attributes can be estimated even for scattering structures that are too small to be resolved with conventional ultrasonic techniques.

The current analysis removed some previous simplifying assumptions we had employed regarding the gating function and beam, both of which had been assumed to be much larger than the effective scatterer dimensions. The analysis still assumes that observations are performed in the transducer's focal zone; when this is not the case, more complex functions are required to describe beam properties, as reported by Waag et al. [27]. In addition, some of the convolution artifacts arising from the gating function may be avoided by incorporating autoregressive spectral-estimation techniques [28].

The *in vitro, in vivo,* and clinical results shown in this report are encouraging. They demonstrate that spectral-parameter imaging could well have a large potential for evaluating therapeutic results in terms of specific morphologic changes induced in treated tissues. We are examining this potential in more detail by
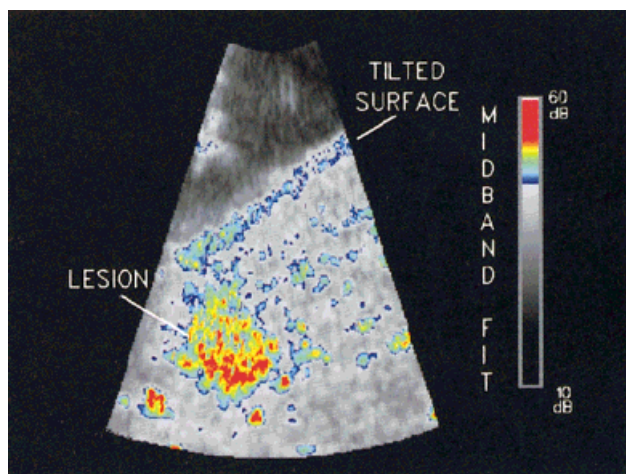

Figure 11. Color coded midband-fit image showing 5-mm focal therapeutic lesion within *in vitro* liver specimen.

comparing 3D results with subsequent histopathology observations. We are also exploring the possibility of on-line parameter imaging so that therapy exposures can be titrated in real time to achieve maximal efficacy and safety.

While this report has addressed ophthalmic applications, the underlying principles and analyses are applicable to assays of other organs. In such applications, attenuation effects require compensation as noted with reference to Equation (1); it may be possible to monitor therapeutic changes (e.g., in liver) without requiring this compensation. To support our studies of other organs, such as the prostate, we have reevaluated Equation (9) using the values of L, q, and frequency ranges that are employed for these examinations. Changing these parameter values alters the numerical coefficients of Equation (9), but it does not change the form of the relationships between spectral parameters and scatterer size and CQ^2. The lower center frequencies employed for organs other than the eye restrict the smallest sizes that can be estimated, and the smaller analysis bandwidths introduce a greater degree of statistical uncertainty in linear regression analysis. Nevertheless, as shown in a companion article [29] in this volume, spectrum analysis results of direct clinical significance can be obtained to complement B-mode examinations of these organs.

ACKNOWLEDGMENTS

REFERENCES

1. G. S. Kino, *Acoustic Waves, Devices, Images, and Analog Signal Processing* (Prentice-Hall, Englewood Cliffs, NJ), 1987.

2. P. S. Magnin, O. T. von Ramm, and F. L. Thurstone. ''Frequency compounding for speckle reduction in phased array images,'' *Ultrasound Imag.* **3**, 267–281 (1982).

3. K. K. Shung and G. Theime, Eds., *Ultrasonic Scattering in Biological Tissues* (CRC Press, Boca Raton), 1993.

4. R. Sigelmann and J. Reid. ''Analysis and measurements of ultrasound backscattering from an ensemble of scatterers excited by sine-wave bursts,'' *J. Acoust. Soc. Am.* **5**, 1351–1355 (1973).

5. I. Y. Kuo and K. K. Shung. ''High-frequency ultrasonic backscatter from erythrocyte suspension,'' *IEEE Trans. Biomed. Eng.* **41**, 29–33 (1994).

6. R. C. Waag, P. P. K. Lee, H. W. Persson, E. A. Schenk, and R. Gramiak. ''Frequency dependent angle scattering of ultrasound by liver,'' *J. Acoust. Soc. Am.* **72**, 343–352 (1982).

7. P. Narayana and J. Ophir. ''On the validity of the linear approximation in the parametric measurement of attenuation in tissues,'' *J. Ultrasound Med. Biol.* **9**, 357–361 (1983).

8. M. O'Donnell, D. Bauwens, J. W. Mimbs, and J. G. Miller. ''Broadband integrated backscatter: An approach to spatially localized tissue characterization *in vivo*,'' *Proc. IEEE Ultrason. Symp.* **79 CH1482-9**, 175–178 (1979).

9. J. G. Mottley and J. G. Miller. ''Anisotropy of the ultrasonic backscatter of myocardial tissue I. Theory and measurements *in vitro*,'' *J. Acoust. Soc. Am.* **83**, 755–761 (1988).

10. L. A. Zagzebski, Z. F. Lu, and L. X. Xao. ''Quantitative ultrasound imaging: *In vivo* results in normal liver,'' *Ultrason. Imag.* **15**, 335–351 (1993).

11. M. F. Insana, J. G. Wood, and T. J. Hall. ''Identifying acoustic scattering sources in normal renal parenchyma *in vivo* by varying arterial and ureteral pressures,'' *Ultrasound Med. Biol.* **18**, 587–599 (1992).

12. E. J. Feleppa, A. Kalisz, J. B. Sokil-Melgar, W. R. Fair, F. L. Lizzi, A. Rosado, M. C. Shao, T. Liu, Y. Wang, M. Cookson, and V. Reuter. ''Typing of prostate tissue by ultrasonic spectrum analysis,'' *UFFC Trans.* **43**, 609–619 (1996).

13. D. L. King, F. L. Lizzi, E. J. Feleppa, P. M. Wai, M. M. Yaremko, M. C. Rorke, and J. Herbst. ''Focal and diffuse liver disease studied by quantitative microstructural sonography,'' *Radiology* **155**, 457–462 (1985).

14. R. E. Parsons, B. Sigel, E. J. Feleppa, M. R. Golub, J. Justin, V. Swami, M. Rorke, A. Kalisz, C. Long, A. Can, and F. L. Lizzi. ''Ultrasonic tissue characterization of experimental venous intimal hyperplasia,'' *Ultrasound Med. Biol.* **19**, 299–308 (1993).

15. M. R. Golub, R. E. Parsons, B. Sigel, E. J. Feleppa, J. Justin, H. A. Zaren, M. Rorke, J. B. Sokil-Melgar, and H. Kimitsuki. ''Differentiation of breast tumors by ultrasonic tissue characterization,'' *J. Ultrasound Med.* **12**, 601–603 (1993).

16. F. L. Lizzi, M. Greenebaum, E. J. Feleppa, M. Elbaum, and D. J. Coleman. ''Theoretical framework for spectrum analysis in ultrasonic tissue characterization,'' *J. Acoust. Soc. Am.* **73**, 1366–1373 (1983).

17. F. L. Lizzi, M. Ostromogilsky, E. J. Feleppa, M. C. Rorke, and M. M. Yaremko. ''Relationship of ultrasonic spectral parameters to features of tissue microstructure,'' *UFFC Trans.* **34**, 319–329 (1987).

18. E. J. Feleppa, F. L. Lizzi, D. J. Coleman, and M. M. Yaremko. ''Diagnostic spectrum analysis in ophthalmology: a physical perspective,'' *Ultrasound Med. Biol.* **12**, 623–631 (1986).

19. D. J. Coleman, R. H. Silverman, M. J. Rondeau, F. L. Lizzi, I. W. McLean, and F. J. Jakobiec. ''Correlation of acoustic tissue typing of malignant melanoma and histopathologic features as a predictor of death,'' *Am. J. Ophthalmol.* **110**, 380–388 (1990).

20. D. J. Coleman, R. H. Silverman, M. J. Rondeau, J. A. Coleman, D. Rosberger, R. M. Ellsworth, and F. L. Lizzi. ''Ultrasonic tissue characterization of uveal melanoma and prediction of patient survival after enucleation and brachytherapy,'' *Am. J. Ophthalmol.* **112**, 682–688 (1991).

21. R. H. Silverman, D. J. Coleman, F. L. Lizzi, J. G. Torpey, J. Driller, T. Iwamoto, S. E. P. Burgess, and A. Rosado. ''Ultrasonic tissue characterization and histopathology in tumor xenografts following ultrasonically induced hyperthermia,'' *Ultrasound Med. Biol.* **12**, 639–645 (1986).

22. E. J. Feleppa and F. L. Lizzi, ''Ophthalmological tissue characterization by scattering,'' in *Ultrasonic Scattering in Biological Tissues.* K. Shung and G. Theime, Eds., CRC Press, Boca Raton, 1993, pp. 393–408.

23. F. L. Lizzi, M. C. Rorke, J. B. Sokil-Melgar, A. Kalisz, and J. Driller. ''Interfacing very-high-frequency transducers to digital-acquisition scanning systems,'' *Proc. SPIE* **1844**, 313–321 (1992).

24. F. L. Lizzi. ''High-precision thermotherapy for small lesions,'' *Eur. Urol.* **23**, 23–28 (1993).

25. D. J. Coleman, R. H. Silverman, T. Iwamoto, F. L. Lizzi, M. J. Rondeau, J. Driller, A. Rosado, D. H. Abramson, and R. M. Ellsworth. ''Histopathologic effects of ultrasonically induced hyperthermia in intraocular malignant melanoma,'' *Ophthalmology* **95**, 970–981 (1988).

26. F. L. Lizzi, D. L. King, M. C. Rorke, et al. ''Comparison of theoretical scattering results and ultrasonic data from clinical liver examinations,'' *Ultras. Med. Biol.* **14**, 377–385 (1988).

27. T. D. Mast and R. C. Waag. ''Wave space resolution in ultrasonic scattering measurements,'' *J. Acoust. Soc. Am.* **98**, 3050–3058 (1995).

28. K. Wear, R. Wagner, and B. Garra. ''High resolution ultrasonic backscatter coefficient estimation based on autoregressive spectral estimation using Burg's algorithms,'' *IEEE Trans. Med. Imag.* **13**, 500–507 (1994).

29. E. J. Feleppa, T. Liu, A. Kalisz, M. C. Shao, W. R. Fair, N. Fleshner, and V. Reuter. ''Ultrasonic spectral-parameter imaging of the prostate,'' *Int. J. Imaging Syst. Technol.* **8**, 11–25 (1997).